Supporting Information for:

Trapping Shape Controlled Nanoparticle Nucleation and Growth Stages via Continuous-Flow Chemistry

Alec P. LaGrow,*[ad] Tabot M. D. Besong,[a] Noktan M. AlYami,[a] Khabiboulakh Katsiev,[b] Dalaver H. Anjum,[c] Ahmed Abd Elkader,[a] Pedro M. F. J. Costa,[a] Victor M. Burlakov,[e] Alain Goriely[e] and Osman M. Bakr*[a]

[a]King Abdullah University of Science and Technology (KAUST), Division of Physical Sciences and Engineering (PSE), Thuwal 23955-6900, Saudi Arabia.

[b]King Abdullah University of Science and Technology (KAUST), SABIC Corporate Research and Innovation Center, Thuwal, 23955-6900, Saudi Arabia.

[c]King Abdullah University of Science and Technology (KAUST), Imaging and Characterization Lab, Thuwal 23955-6900, Saudi Arabia.

[d]JEOL Nanocenter and Department of Physics, University of York, Heslington, York YO10 5DD, U.K.

[e]Mathematical Institute, University of Oxford, Woodstock Road, Oxford OX2 6GG, U.K.

Table of Contents

1. Experimental Section:

Chemicals. Toluene, and tungsten carbonyl (97%) were purchased from Sigma Aldrich. Cobalt (III) acetylacetonate (98%), nickel (II) acetylacetonate (95%), and platinum (II) acetylacetonate (98%) were purchased from STREM. Oleylamine (technical grade, 70%), 1-adamantane carboxylic acid (99%), and copper (II) acetylacetonate (98%), were purchased from Acros Chemicals. Absolute ethanol was ordered from VWR. All chemicals were used as delivered without further purification. Nickel acetylacetonate was weighed as the dihydrate.[1]

Synthetic Procedures. Reactions were carried out in the FlowSyn Multi X, commercially available from Uniqsis Ltd, fitted with a 1 mL stainless steel coil reactor, with a 1/16th inch (1.5875 mm) diameter, and a 10 bar inert back pressure regulator supplied by Uniqsis. The precursor and surfactant solution consisting of $Pt(acac)_2$ (0.01 $molL^{-1}$), $Ni(acac)_2.2H_2O$ (0.01 $molL^{-1}$), 1-adamantanecaboxylic acid (0.02 $molL^{-1}$), and oleylamine (0.2 $molL^{-1}$) dissolved in toluene was flowed through pump A. The reducing agent solution consisted of $W(CO)_6$ (0.03 $molL^{-1}$) dissolved in toluene was flowed through pump B. Both pumps were set to the same flow rate to give a set residence time (5, 7.5, 10, and 20 seconds). Once the pressure reached equilibrium at 10 bar, the reaction was started. The solutions were not degassed before introduction to the flow reactor. The precursor solution and reducing agent solution were mixed in a mixing device and then injected into the coil reactor, preheated to 240 °C. Before collecting the product, the solution containing the particles was run through a 200 µL coil mounted in a cooled stainless steel block that was kept at 20 °C and acts as a heat sink. This allowed the solution to be cooled by over 180 °C in less than a second (as measured from the solutions upon exiting the reactor). The resulting solution was mixed with 80% ethanol and precipitated by centrifugation at 15,000 rpm for 1 hour. The supernatant was discarded and the precipitates were re-dispersed in toluene and washed again with ethanol as the anti-solvent. After the particles were cleaned by centrifugation at least three times they were re-suspended in toluene and deposited on to copper TEM grids.

For the pure platinum and the platinum alloys the same conditions were used but replacing $Ni(acac)_2.2H_2O$ with $Pt(acac)_2$, $Cu(acac)_2$, and $Co(acac)_3$, respectively. The times used were 10 seconds for platinum and

platinum copper, and 5 seconds for platinum cobalt. The final time of the particles was 7.5 minutes for all samples.[2]

The supernatant was removed from the products immediately to keep the tungsten in solution. Inductively coupled plasma optical emission spectrometry (ICP-OES) was carried out on a Varian 720-ES ICP-optical emission spectrometer to determine if the tungsten was left in solution, and it was found that the tungsten was over 600 times as prevalent in the solution as the precursor metals (after 7.5 minutes of reaction). The solution for ICP-OES was prepared by drying the supernatant and dissolving in a mixture of 1 mL of nitric acid, 3 mL of hydrochloric acid, and 1 mL of hydrofluoric acid. 1 mL of the acidified solution was diluted with 9 mL of dilute nitric acid and run for ICP-OES.

The remaining tungsten was studied with X-ray photoelectron spectroscopy and was determined to be in its fully oxidized form (W^{6+}) (Figure S1).

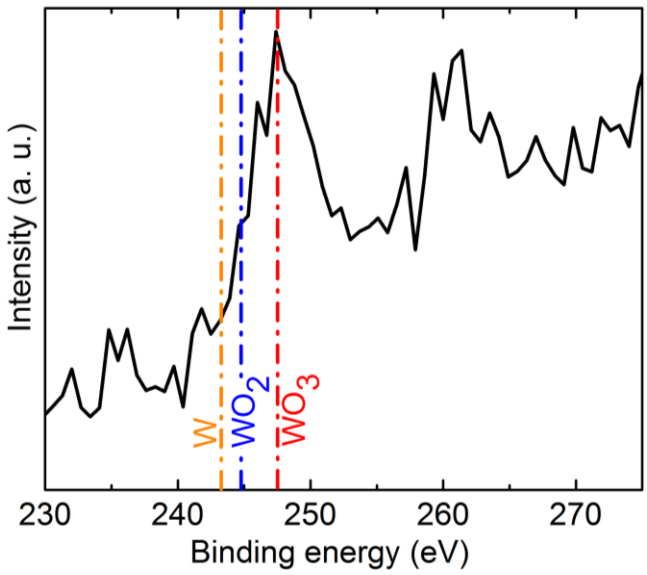

Figure S1. XPS spectra of the W 4d core levels of the left over tungsten, with guides showing standard values for W, WO_2 (W^{4+}) and WO_3 (W^{6+}).

X-ray photoelectron spectroscopy. XPS experiments were carried out with Scienta R3000 electron spectrometer and SPECS XR-50 Al K(alpha) X-ray source. The X-ray power of 375 W at 10 kV was used for all experiments. Instrument base pressure was ca. 1 x 10^{-9} Torr. All the acquired spectra were referenced to C 1s line of adventitious (aliphatic) carbon. All the spectra were collected at room temperature. All XPS spectra were recorded using IGOR software and processed using CasaXPS v.2.3.14.

Analytical Ultracentrifugation. All sedimentation velocity (SV) experiments were carried out on a Beckman Optima XL-A analytical ultracentrifuge (AUC) equipped with scanning absorption optics using a standard double sector cell with titanium centerpieces assembled with quartz windows and an AnTi-60 rotor. All measurements were made at 420 nm, at 20 °C, at speeds ranging from 6,000 rpm to 30,000 rpm. At least 100 scans were used in data analysis using Ultrascan 3.3 revision 1901 with enhanced Van Holde-Weichet Analysis (vHW)[3] employing at least 90% of the boundary region and a smoothing factor of 10 or less for all datasets. SV data was also fitted with the 2-Dimensional Spectrum Analysis model to determine the sedimentation and diffusion coefficients (*s* and *D* values) and the frictional ratios (f/f_o). SV runs typically required 0.05 to 0.5mg of material in 400µL toluene. Each sample was prepared at varying concentrations to ensure that the sedimentation and diffusion coefficients were not concentration dependent. An inhomogeneous solvent model was applied to account for solvent compressibility caused by high pressure build-ups at the centrifugal fields obtained at high rotor speed.

Electron Microscopy. Bright field transmission electron microscopy (BF-TEM) was carried out on FEI Titan 80-300 ST equipped with an extra-brightness field emission gun (x-FEG). The energy dispersive X-ray spectroscopy (EDS) was taken with a liquid nitrogen cooled detector from EDAX, Inc., with a lithium doped silicon diode, a beryllium window, and an optimized solid angle of 0.07 stradians. The EDS acquisition was taken at the optimized tilt angle of +14°. The EDS ratios were taken from multiple areas and over a thousand particles.

The aberration corrected high angle annular dark field scanning transmission electron microscopy (HAADF-STEM) was carried out on a FEI Titan 80-300 ST equipped with a spherical aberration corrector on

the probe, with a 20 mrad or better phase space, to achieve sub-angstrom spatial resolution. The microscope was also equipped with an energy filter of model GIF Quantum 966 from Gatan, Inc. to investigate the materials with electron energy-loss spectroscopy (EELS) technique. All electron microscopy analysis was carried out with an accelerating voltage of 300 kV.

STEM-EELS spectrum imaging (SI) was utilized to generate the elemental maps of the alloy nanoparticles. A GIF Quantum 966 was used to acquire the STEM-EELS datasets with a typical exposure time of 10 ms and collection angle of 30 mrad. The elemental maps were generated with the Pt-O (52 eV) edge for platinum in all cases, and the other metals used the Ni-M (68 eV), Cu-M (73 eV), and Co-M (63 eV) edges respectively. Multiple Linear Least Square (MLLS) method have been applied to SI datasets in order to generate the de-convoluted maps of Pt and Ni, Cu or Co. Finally, the entire data collection as well as analysis have been completed in Gatan Microscopy Suite (GMS) of version 2.3.

The HAADF-STEM was performed with a 70 µm condenser aperture and a camera length of 185 mm. High resolution STEM analysis of the particles below 2 nm was carried out by focusing on a nearby area and then moving the sample, with the beam off, to a new area. The images were immediately recorded, as the beam was exposed to the sample, with a 4 µs scan speed. For the particles below 2 nm, the images used for analysis were taken from the first scan. The particle measurements were done by measuring the edge length, or otherwise the diameter. Over 500 particles of each sample were studied.

To minimize surface rearrangement and aggregation of the nanoparticles below 2 nm the exposure to the electron beam was minimized to occur only during image acquisition. It should be noted that, in all cases where nanoparticles were 5 nm or below, any particle that was physically touching other(s) rapidly underwent rearrangement and coalescence. Because of this, the nanoparticles that were imaged for analysis and discussed in the text were all physically isolated. Due to the ability of the surface atoms to diffuse the nanoparticles were studied for up to 10 seconds. During this interval of time, limited rearrangement was observed (Figure S2-S4). The images taken within the first 3 seconds were considered to be the initial state.

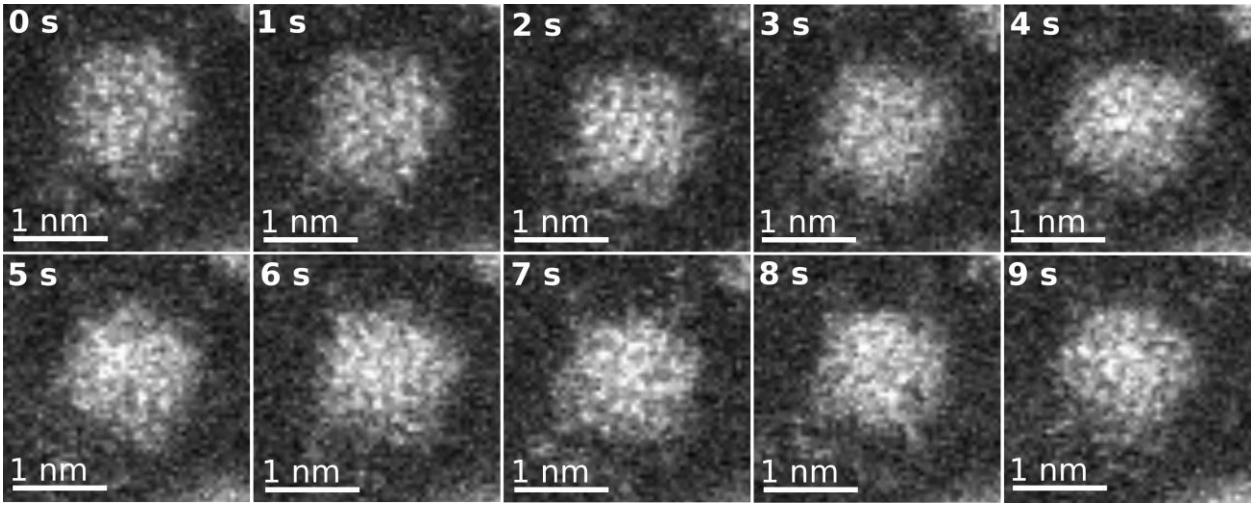

Figure S2. Isolated platinum nickel nanoparticles formed after 5 seconds and imaged at 300 kV. Time 0 was counted as the initial exposure and then the particles were imaged with consecutive 1 second exposures.

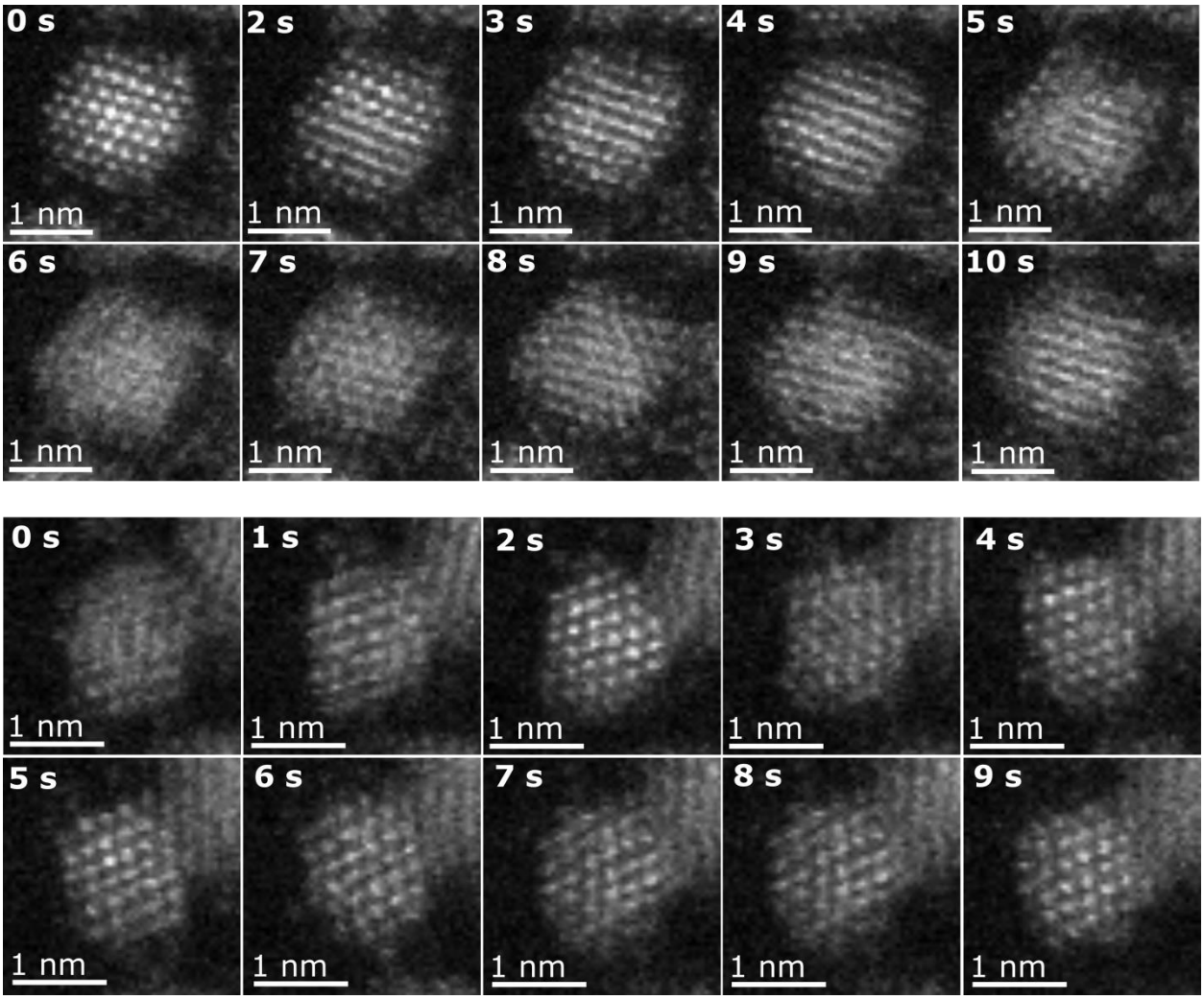

Figure S3. Isolated platinum nickel nanoparticles formed after 7.5 seconds and imaged at 300 kV. Time 0 was counted as the initial exposure and then the particles were imaged with consecutive 1 second exposures.

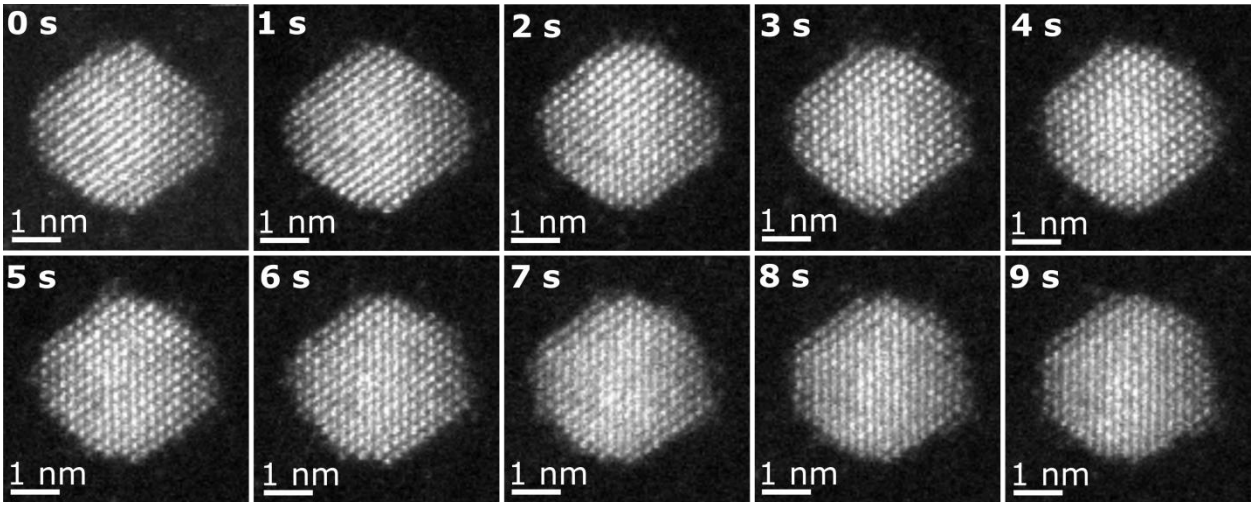

Figure S4. Isolated platinum nickel nanoparticles formed after 10 seconds and imaged at 300 kV. Time 0 was counted as the initial exposure and then the particles were imaged with consecutive 1 second exposures.

2. Nanoparticle Characterization:

Table S1. The average EDS measurement ratio of the platinum nickel particles in Figure 1. The atomic percentage EDS ratios were taken from areas containing over a hundred particles in each acquisition and were averaged over multiple acquisitions cumulatively studying over a thousand particles. The averaging of the multiple measurements gives the uncertainties used in the table by taking the standard deviation of the measurements.

Time (s)	Measured Pt (EDS)	Measured Ni (EDS)
5	72 ± 3 %	28 ± 3 %
7.5	82 ± 3 %	18 ± 3 %
10	54 ± 2 %	46 ± 2 %
20	47 ± 2 %	53 ± 2 %

The nanoparticles produced with a residence time of 5 seconds were seen to be poorly crystalline or disordered at smaller sizes and ordered at sizes of around 1.3 nm and above (Figure S1).

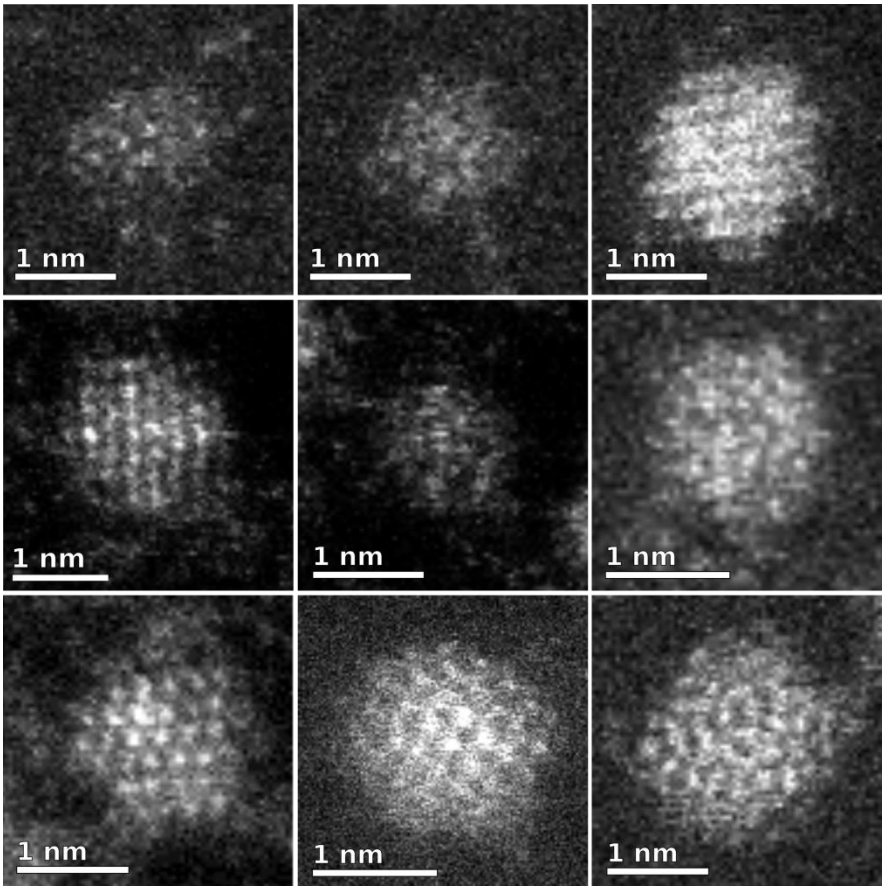

Figure S5. High resolution HAADF-STEM images of platinum-nickel formed after a 5 second reaction time.

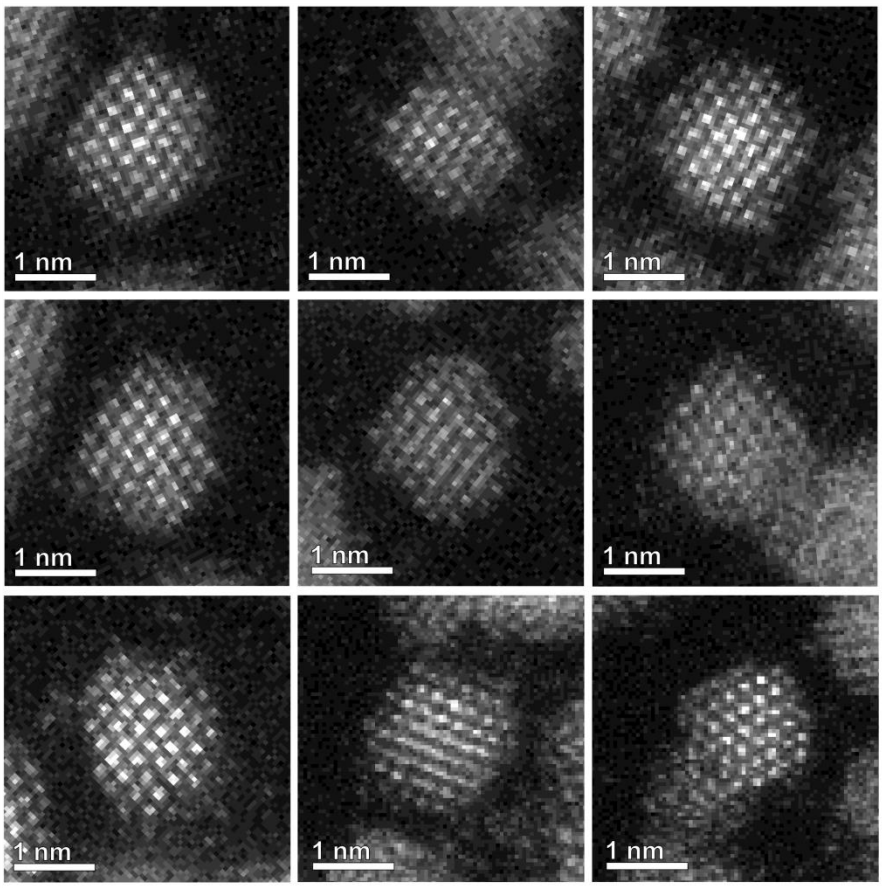

Figure S6. High resolution HAADF-STEM images of platinum-nickel formed after a 7.5 second reaction time.

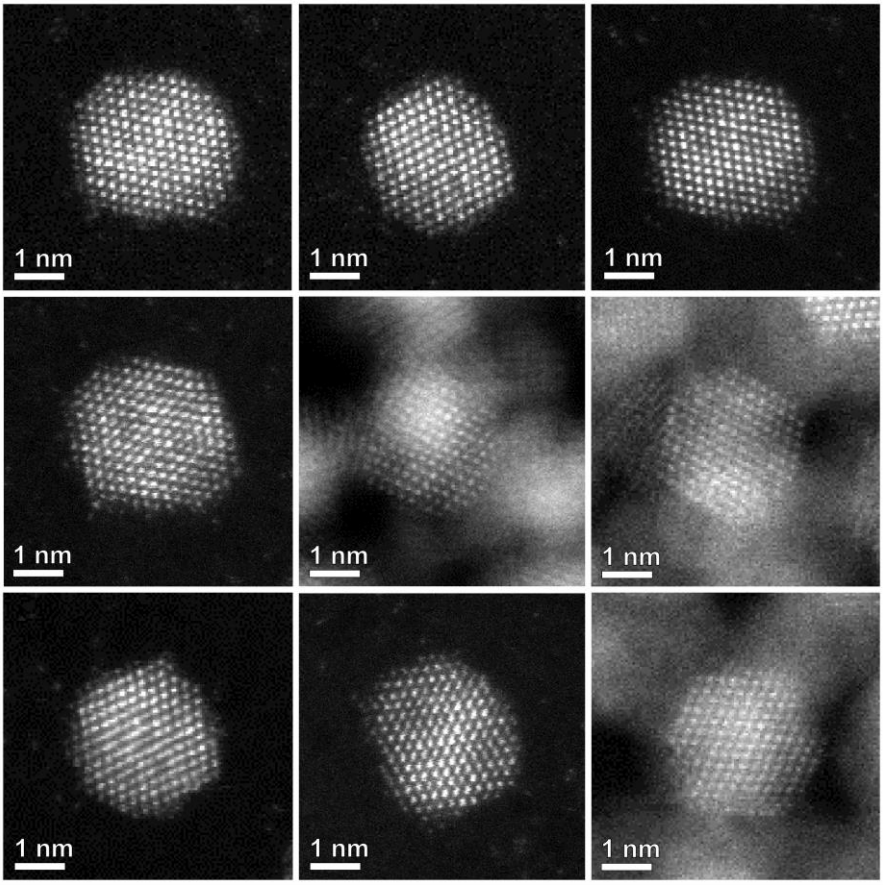

Figure S7. High resolution HAADF-STEM images of platinum-nickel formed after a 10 second reaction time.

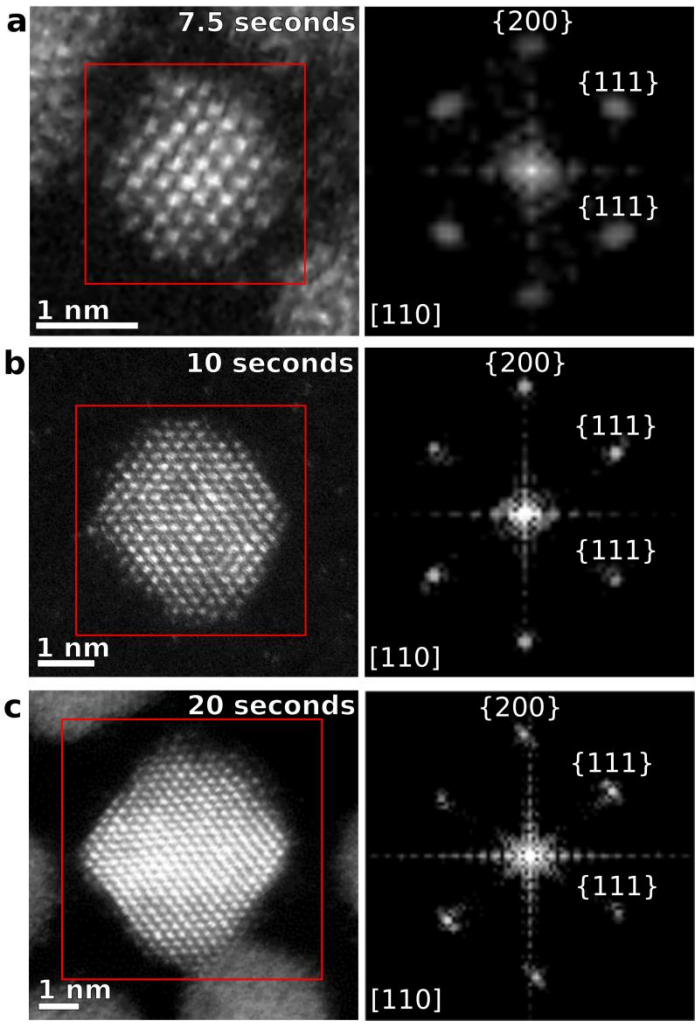

Figure S8. HAADF-STEM images of the platinum nickel nanoparticles shown in Figure 1 of the manuscript and the FFT patterns and assignments used.

The XRD of the nanoparticle alloys show a shift in the peak position from being platinum rich to being nickel rich as well as a sharpening as it moves from 7.5 seconds to 20 seconds, with 5 seconds being slightly less platinum rich than at 7.5 seconds, consistent with the EDS (Figure S9 and Table S2).

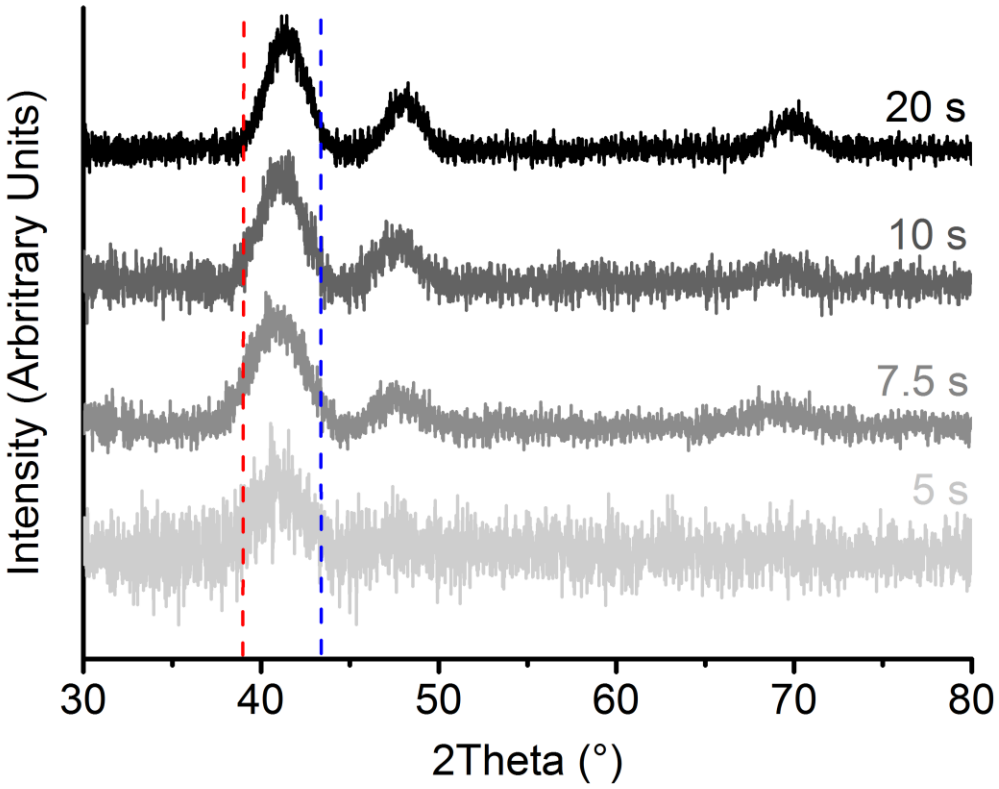

Figure S9. XRD profiles of the nanoparticles formed after 5, 7.5, 10 and 20 seconds. The red and blue dashed lines indicate the positions of the (111) peaks of platinum and nickel respectively.

Table S2. The particle size obtained from the XRD with the Scherrer equation.

Time (s)	Particle Size (XRD)
5	1.9 ± 0.9 nm
7.5	2.0 ± 0.5 nm
10	2.6 ± 0.4 nm
20	3.3 ± 0.3 nm

3. Modelling of Nanoparticle Growth

3.1. Crystalline versus amorphous structure of small nanoparticles

Small particles have a significant fraction of their atoms on surfaces. The energy associated with the under-coordination of the surface atoms is defined as the surface energy and makes an important contribution to the total free energy of particles. The value of surface energy strongly depends on crystallographic orientation of the surface. For Pt, for instance, the surface energy per atom is ~1 eV, ~1.4 eV, and ~2 eV for {111}, {100} and {110} crystal facets, respectively.[4] Similarly for Ni, the corresponding energies are ~0.7 eV, ~1 eV, and ~1.3 eV. Minimization of the total surface energy is therefore driven by two competing tendencies: 1) minimization of the total surface area and 2) maximization of the surface area fraction covered with the low-energy facets. Considering the bulk and surface contribution to the total energy we can qualitatively explain the sequence of particle shapes upon nucleation and subsequent growth along the following lines.

The total energy of as-nucleated particles is positive and equal to the value of nucleation barrier (see S2 for details) because the main contribution comes from the surface energy. As the contribution of the particle interior to the total energy is relatively small, the energy minimum can be reached by creating bulk defects, i.e. twinning,[5] slightly increasing the bulk energy due to elastic stresses but allow minimizing surface energy. The latter can be achieved by minimizing the surface area (the particles' shape is close to spherical) and covering it with the lowest energy {111} facet.

As the particles grow the contribution of its interior to the total energy becomes more important than that of the surfaces, i.e. the bulk defects become more energetically expensive. This drives the particle to get rid of bulk defects and adopt the shape to expose the lowest energy {111} facets (octahedron) or a mixture of {111} and {100} facets (truncated octahedron) on its surfaces. Relative energetics of the larger particles with different shapes is presented in the work of Wen *et al*.[6]

In the case of alloy particles there is an extra parameter affecting the surface energy, namely the composition, as nucleated particles usually form disordered alloys.[5] Besides, they

may have different average composition with one component concentration noticeably exceeding the other and the average concentration of solution. According to Burlakov and Kantorovich,[7] the composition evolution of the alloy particles is much faster than that of their size distribution and relatively quickly reaches quasi equilibrium distribution $x(R) = x_0 + \delta / R$ for the component with higher cohesive energy (in our case this is Pt with $\varepsilon_{Pt} = 5.85$ eV/atom; compared to 4.44 eV/atom for Ni). This distribution indicates a higher content of the Pt component in smaller particles. Such effect can be understood recalling that the atomic incoming fluxes to the particle for Pt and Ni are approximately the same (equal initial concentrations in the solution) while the outgoing fluxes are controlled by the detachment rates proportional to $\exp(-\varepsilon_C / k_B T)$ with ε_C being the corresponding cohesive energy. As the particle distribution grows further the accumulation of one component in smaller particles creates a deficit of this component in the solution such that the larger particles eventually adopt the average overall composition, i.e. close to 50%, the result observed in our experiments.

3.2. Surface energy and nucleation barrier for nanoparticles

We consider the free energy of a system containing a single nucleated particle and the atoms dissolved in a solution with a given solvation energy ε_S

$$\begin{aligned} G = &-\varepsilon_C n_{\mathrm{P}} + \gamma \cdot S_{\mathrm{P}} - \varepsilon_{\mathrm{S}} \cdot n_{\mathrm{A}} + T n_{\mathrm{A}} \cdot \ln\left(n_{\mathrm{A}} v_{\mathrm{A}}\right) + T n_{\mathrm{S}} \cdot \ln\left(n_{\mathrm{S}} v_{\mathrm{S}}\right) \\ &-T \cdot \left(n_{\mathrm{A}} + n_{\mathrm{S}}\right) \cdot \ln\left(n_{\mathrm{A}} v_{\mathrm{A}} + n_{\mathrm{S}} v_{\mathrm{S}}\right) \end{aligned}, \qquad \text{(S1)}$$

where ε_C is the cohesive energy of atoms in the particle, γ is the surface energy per atom, n_A and n_S are the concentrations of atoms and of solvent molecules in the solution, respectively, S_{P} is the number of atoms on the surfaces of the particle, T is the solution temperature and v_{S} and v_{A} are the characteristic volumes of the solvent molecule and the atom, respectively. It is convenient to introduce the total concentration of atoms $m_{\mathrm{A}} = n_{\mathrm{A}} + n_{\mathrm{P}}$. Expressing n_{A} in terms of the total concentration allows us to rewrite Equation (S1) in the form

$$G = -\varepsilon_C n_{\mathrm{P}} + \gamma \cdot S_{\mathrm{P}} - \varepsilon_S \cdot \left(m_A - n_P\right) + T\left(m_{\mathrm{A}} - n_{\mathrm{P}}\right) \cdot \ln\left(\left(m_{\mathrm{A}} - n_{\mathrm{P}}\right) v_{\mathrm{A}}\right)$$
$$+ T n_{\mathrm{S}} \cdot \ln\left(n_{\mathrm{S}} v_{\mathrm{S}}\right) - T\left(m_{\mathrm{A}} + n_{\mathrm{S}} - n_{\mathrm{P}}\right) \cdot \ln\left(v_{\mathrm{A}} m_{\mathrm{A}} + v_{\mathrm{S}} n_{\mathrm{S}} - v_{\mathrm{A}} n_{\mathrm{P}}\right) \quad \text{(S2)}$$

We are interested in the equilibrium (critical) size of the particle when the atomic concentration $n_A << n_S$ and does not change significantly in a single nucleation event

$$\frac{\partial G}{\partial n_{\mathrm{P}}} = \varepsilon_S - \varepsilon_C + \gamma \cdot \frac{dS_{\mathrm{P}}}{dn_P} - T \cdot \ln\left(\frac{n_A v_{\mathrm{A}}}{v_{\mathrm{S}} n_{\mathrm{S}}}\right) = 0 \quad \text{(S3)}$$

In order to calculate the derivative dS_{P} / dn_P, we need to specify the particle shape. We assume here that the particle is spherical and note that any deviation from sphericity can be taken into account by a modification of the surface energy such that $\gamma \le \gamma_{nsp}$, where γ_{nsp} is the surface energy of a non-spherical particle. Using the spherical assumption Eq. (S3) becomes

$$\varepsilon_S - \varepsilon_C + \frac{2\gamma}{R_{cr}} - T \cdot \ln\left(n\right) = 0,\ n = \frac{n_A v_{\mathrm{A}}}{n_S v_{\mathrm{S}}} \quad \text{(S4)}$$

From this last expression, we obtain the critical radius

$$R_{cr} = \frac{2\gamma}{\varepsilon_C - \varepsilon_S + T \cdot \ln\left(n\right)} \quad \text{(S5)}$$

The nucleation barrier corresponds to the energy required to transfer atoms from solution to create the particle of radius R_{cr}, i.e.

$$\Delta = G\left(R = R_{cr}\right) - G\left(R = 0\right) = \frac{16\pi\gamma^3}{3\left(\varepsilon_C - \varepsilon_S + T \cdot \ln\left(n\right)\right)^2} \quad \text{(S6)}$$

Eq. (S6) shows that the nucleation process strongly depends on the surface energy γ of the material and on its cohesive energy relative to the atomic free energy in the solution

$$\varepsilon_C - \varepsilon_S + T \cdot \ln\left(n\right) \quad \text{(S7)}$$

4. Analytical ultracentrifugation:

The sedimentation velocity data was analyzed with the Ultrascan 3 analysis package employing 2 different widely used models of data analysis in analytical ultracentrifugation - 2-Dimensional Spectrum Analysis (2-DSA) and the enhanced van Holde-Weichet Analysis (vHW).[3, 8] 2-DSA is a model-independent analysis method, which fits the sedimentation velocity data to determine the sedimentation and diffusion coefficients as well as both the shape and molecular weight distributions of mono- and polydisperse solutions of macromolecules, such as nanoparticles. The vHW analysis is a model-independent approach to sedimentation velocity analysis, whereby, the sedimentation and diffusion processes are de-convoluted by plotting the apparent sedimentation coefficient values against the reciprocal of the square-root of time and extrapolating to infinity (vertical-intercept). Briefly, the velocity profiles resulting from sedimentation are discretized evenly between the baseline and stable plateau regions (Figure S10 **a**), from which the apparent sedimentation coefficient values (*s**) are computed using Equation S8.

$$s^*_{i,b} = \frac{1}{\omega^2 (t_i - t_0)} \ln\left[\frac{r_b(t_i)}{r_M(t_0)}\right] \qquad \text{(S8)}$$

where ω^2 is the angular velocity, (t_i - t_0) is the effective centrifugation time (t_0 being the start time of centrifugation corrected for rotor acceleration and t_i the total centrifugation time),[9] r_M and r_b are the radial positions of the meniscus and the cell base of the AUC cell, respectively. A regression plot of apparent sedimentation coefficient values against the reciprocal of the square-root of the time of centrifugation is then constructed and extrapolated to infinite time (Figure S10 **b**). The manner in which the regression lines intersect at the vertical axis is diagnostic of sample heterogeneity. Intersection at a single point indicates molecular monodispersity, while intersection at several points is reflective of a distribution of soluble/dispersible molecular components. Integral sedimentation coefficient distribution plots (Figure S10 **c**) can be obtained from plotting the boundary fractions against the sedimentation coefficients. In addition, a histogram distribution (Figure S10 **d**) can also be obtained via binning the sedimentation coefficients and calculating their corresponding frequencies.

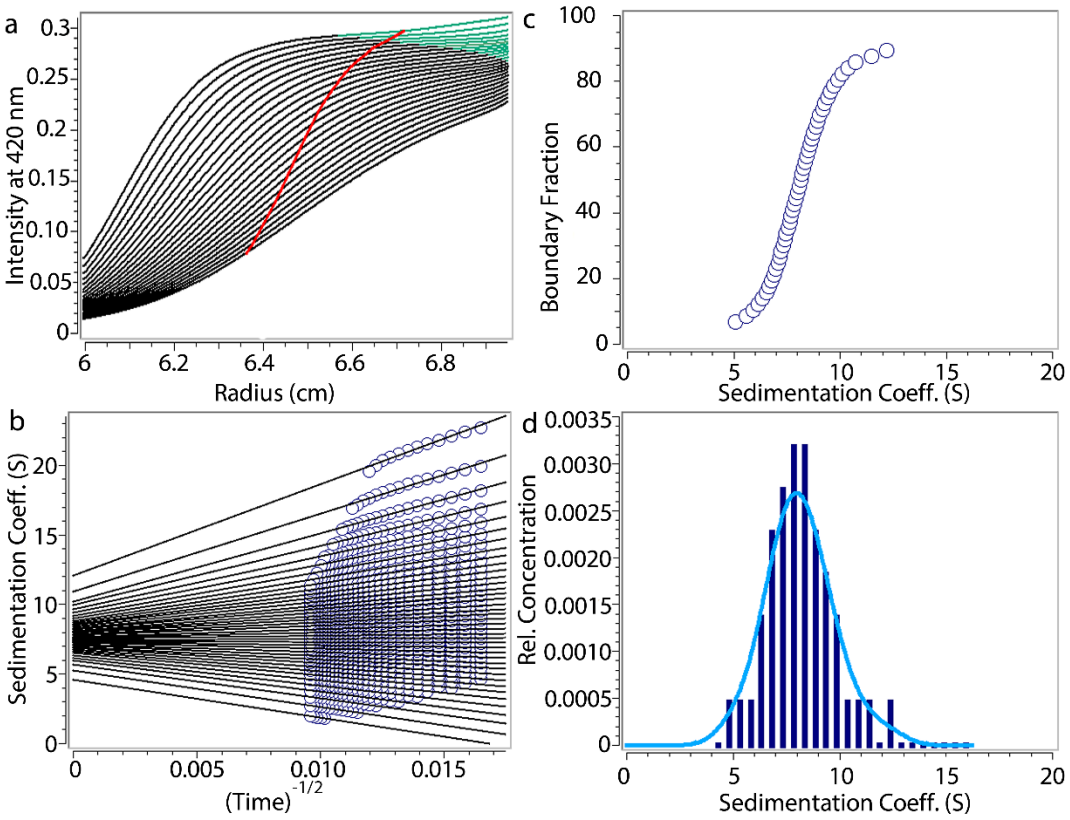

Figure S10. Enhanced van Holde-Weichet analysis of sedimentation velocity data obtained for platinum nickel nanoparticles in toluene. (a) Representative sedimentation velocity profiles with the red curve showing the diffusion tolerance, (b) extrapolation plot, (c) integral plot of apparent S-values, (d) histogram plots of apparent S-values for platinum nickel nanoparticles after 5 seconds through the reactor.

Multiple speeds (from 6000 – 30000 rpm) were employed over a number of runs for each of the samples and a suitable speed was subsequently determined for each sample in order to collect optimum data for diffusion and sedimentation processes. This is mainly because employing a very low speed will often result in incomplete sedimentation, which limits the amount of information to be obtained from the data as diffusion becomes more dominant towards the end of the run. On the other hand, employing too high a speed causes sedimentation to occur very rapidly and most of the sedimentation data is lost before it can be captured. Accordingly, a rotor speed of 8000 rpm was employed for the sample with a 20 second residence time, 12000 rpm for the sample with a 10 second residence time, 21000 rpm for the sample

with a residence time of 7.5 seconds and 25000 rpm for the sample with a residence time of 5 seconds. The results are summarized in table S3 and S4.

Subjecting a nanoparticle solution to appropriate centrifugal forces brings about sedimentation, and the corresponding sedimentation coefficient distribution obtained is a fundamental property of the nanoparticle assembly. Sedimentation coefficient values are generally reported in Svedberg (S) or in seconds (s), where $1S = 10^{-13}s$. A typical van Holde – Weichet analysis of the sedimentation velocity data after 5 seconds have a distribution of sedimentation coefficients ranging from 5.4 S to 11.4 S with an average sedimentation coefficient of 8.0 S (Table S5). The sedimentation coefficients show a Gaussian distribution with tails towards larger S values, suggesting the presence of minute amounts of larger components. This is consistent with a system that exhibits growth and similar results were obtained when the growing platinum-nickel were trapped in solution after 7.5, 10, and 20 seconds (Figure S11). The sedimentation coefficients were not observed to vary significantly with concentration (Table S5-S8), thereby ruling out any incidence of reversible self-association within the nanoparticle preparations and further confirming continuous growth of the platinum-nickel nanoparticles with increasing residence times in the flow reactor. The raw sedimentation velocity data was also fitted to a 2-dimensional spectrum analysis (2-DSA) model with 70 Monte Carlo iterations in the Ultrascan software (Ultrascan 3.3, revision 1901).[10] In addition to the sedimentation and diffusion coefficients, the average molecular weight and hydrodynamic diameter of the platinum-nickel nanoparticles (most abundant component of the distribution) were determined as previously reported.[11] The results are presented in Table S3 and are largely in agreement with the TEM results depicting an increase in nanoparticle diameter with increasing residence times. It should be noted that the thickness of the ligand shell is incorporated into the average hydrodynamic diameter of the nanoparticle (particle diameter), while the average particle diameter from TEM is only for the core of the platinum nickel nanoparticle.

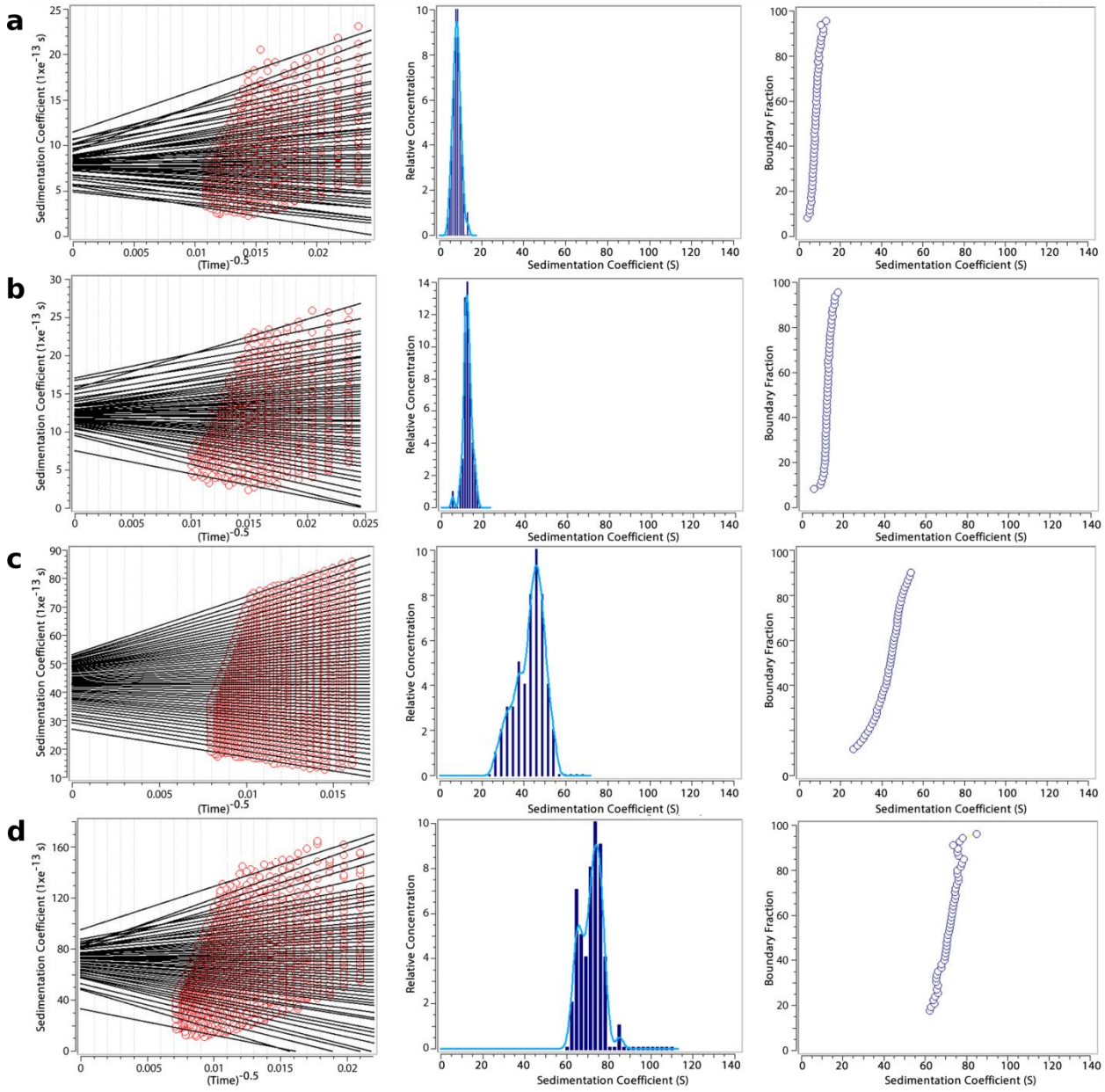

Figure S11. van Holde-Weichet (vHW) analysis of sedimentation velocity data for platinum nickel nanoparticle samples at different times: (a) 5 s, (b) 7.5 s, (c) 10 s, and (d) 20 s.

Table S3. Summary of Sedimentation Velocity (2-Dimensional Spectrum Analysis or 2-DSA model) for the main component of the platinum nickel samples with residence times from 5 seconds to 20 seconds.

Time (s)	$s_{20,Toluene}$ (S)	$s_{20,w}$ (S)	$D_{20,Toluene}$ (x 10^{-6} cm^2/s)	$D_{20,w}$ (x 10^{-6} cm^2/s)	Solvated Diameter (nm)	Molecular Weight (Da)	Density (g/cm^3)
5	13.5 ± 0.1	7.9 ± 0.1	3.2 ± 0.4	1.9 ± 0.3	2.3 ± 0.3	32800 ± 2700	3.7 ± 0.8
7.5	18.4 ± 0.1	10.7 ± 0.1	2.6 ± 0.1	1.6 ± 0.1	2.7 ± 0.1	40600 ± 1500	3.4 ± 0.2
10	93.6 ± 4.8	54.6 ± 2.7	1.2 ±0.1	0.7 ± 0.1	5.9 ± 0.5	243500 ± 21500	3.1 ± 0.3
20	116.8 ± 8.1	67.8 ± 4.7	1.0 ± 0.1	0.6 ± 0.2	7.5 ± 0.4	400925 ± 30976	3.0 ± 0.2

Table S4. Summary of sedimentation velocity (vHW method) analysis for the platinum nickel samples at the same concentration ([OD]) and different residence times.

Time (s)	Conc [OD]	$s_{av.}$ (S)	%	$s_{low\ limit}$ (S)	%	$s_{upper\ limit}$ (S)	%
5	0.45	8.0	88.0	5.4	4.0	11.4	8.0
7.5	0.45	12.0	84.0	8.5	4.0	14.9	12.0
10	0.45	45.7	80.0	28.5	10.0	57.3	10.0
20	0.45	72.8	86.0	49.5	4.0	90.1	10.0

Table S5. Sedimentation coefficients of the platinum nickel nanoparticle solution after 5 seconds against their concentration.

Conc [OD]	$S_{av\text{-(distr)}}$(S)	$S_{abudant\ species}$ (S)
0.29	8.13	8.4
0.45	7.80	7.62
0.58	7.86	8.14
0.63	8.17	8.57
1.05	8.04	7.61
Average	**8.0**	**8.1**
Standard Deviation	**0.2**	**0.4**

Table S6. Sedimentation coefficients of the platinum nickel nanoparticle solution after 7.5 seconds against their concentration.

Conc [OD]	$S_{av\text{-(distr)}}$(S)	$S_{abudant\ species}$ (S)
0.29	12.57	12.54
0.45	12.24	12.24
0.58	12.33	12.48
0.63	12.76	12.67
1.05	12.38	12.57
Average	**12.5**	**12.5**
Standard Deviation	**0.2**	**0.2**

Table S7. Sedimentation coefficients of the platinum nickel nanoparticle solution after 10 seconds against their concentration.

Conc [OD]	$S_{average\ (distribution)}$(S)	$S_{abudant\ species}$ (S)
0.29	47.48	47.32
0.45	45.78	46.24
0.58	45.44	42.91
0.63	46.24	45.63
1.05	46.02	45.83
Average	**46.2**	**45.6**
Standard Deviation	**0.8**	**1.6**

Table S8. Sedimentation coefficients of the platinum nickel nanoparticle solution after 20 seconds against their concentration.

Conc [OD]	$S_{average}$ (distribution)(S)	$S_{abudant\ species}$ (S)
0.29	66.21	68.15
0.45	72.58	68.5
0.58	67.10	66.87
0.63	72.47	74.33
1.05	72.23	83.42
Average	**70.1**	**72.3**
Standard Deviation	**3.2**	**6.9**

4. Spectroscopy

4.1. Fourier Transform Infrared Spectroscopy (FTIR)

FTIR spectra of platinum-nickel nanoparticles were acquired using the Nicolet iS10 FTIR spectrometer (Thermo Scientific) in reflection mode. 32 scans were acquired for each time point in transmittance mode with 3 repeats. Samples were thoroughly washed with toluene/ethanol solutions and centrifuged at 24,100 x g for 20 mins (5 – 6 cycles). The resulting pellets were re-dissolved in DCM and dried in a fume hood at room temperature shortly before measurements.

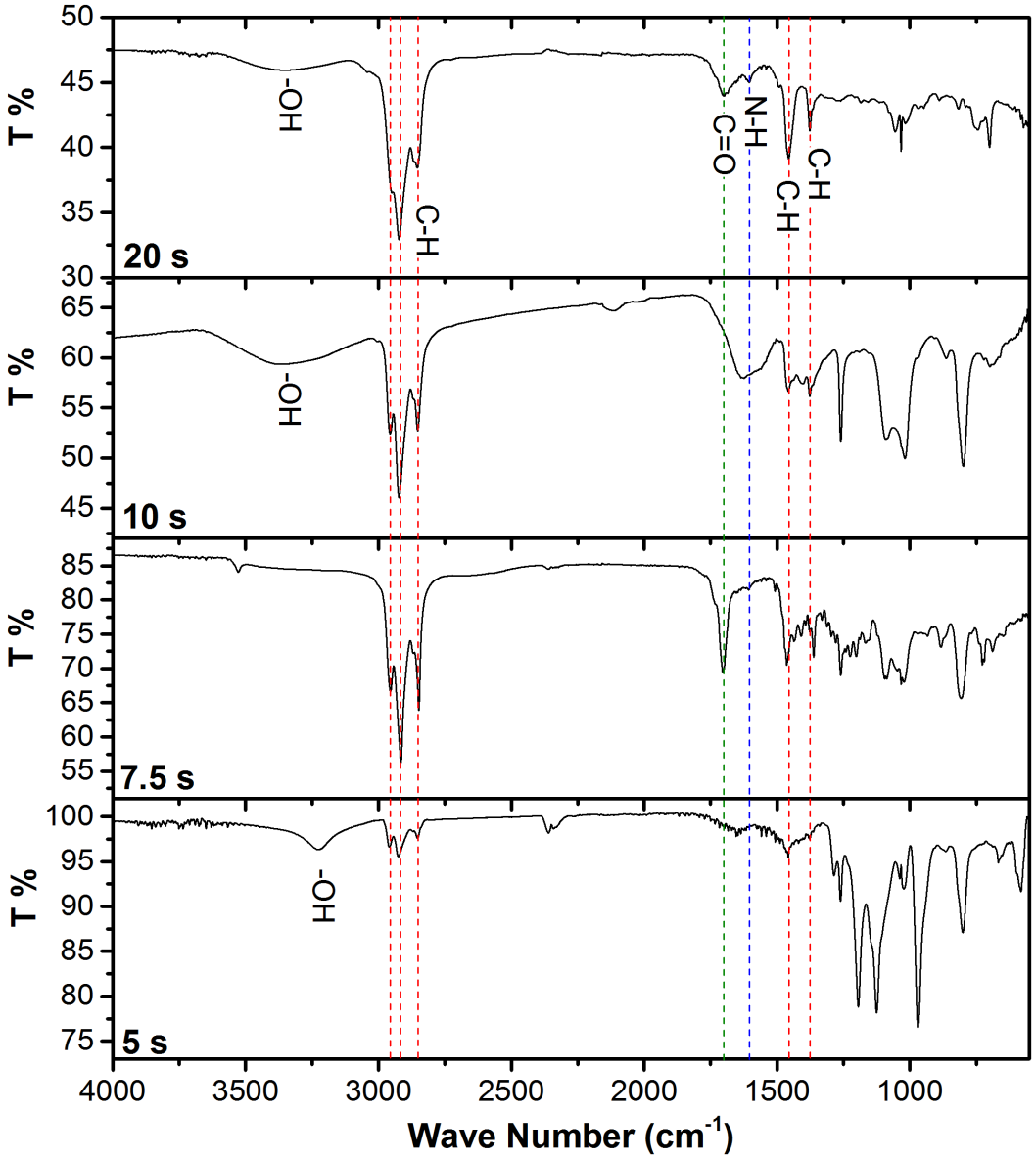

Figure S12. FTIR spectra of platinum-nickel nanoparticles formed after 5, 7.5, 10 and 20 seconds. Alkane C-H stretches are marked with red dashes, the major C=O stretch is marked with a green dashes and the N-H stretch is marked with blue dashes.

The major peaks in the 5 second sample in Figure S12 are 3227, 2956, 2924, 2851, 1288, 1258, 1197, 1128, 971, 802, 644, and 576 cm^{-1}, in the 7.5 second sample they are 3529, 2956, 2916, 2851, 1697, 1467, 1362, 1092, 1024, 890 cm^{-1}, in the 10 second sample they are 3368, 2955,

2924, 2851, 1633, 1451, 1370, 1258, 1092, 1015, 797 cm^{-1} and in the 20 second they are 3368, 2970, 2851, 1701, 1608, 1455, 1379, 1055, 1031, 749, 700 cm^{-1}.

4.2. X-ray Photoelectron Spectroscopy (XPS)

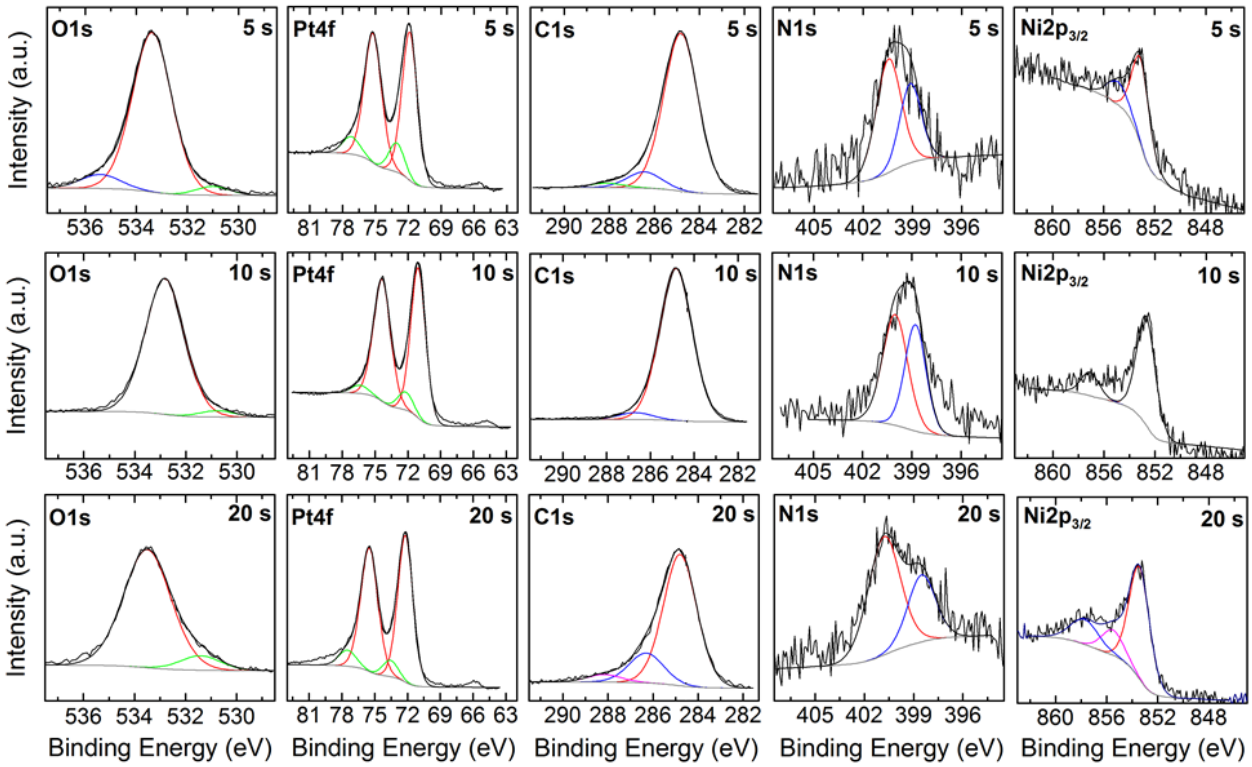

Figure S13. XPS spectra of the O 1s, Pt 4f, C 1s, N 1s and Ni $2p_{3/2}$ core levels of platinum-nickel nanoparticle samples at 5, 10 and 20 seconds.

Table S9. Values of the peaks fit to the X-ray Photoelectron Spectroscopy (XPS) in Figure S13 of platinum nickel nanoparticle samples at 5, 10 and 20 seconds of the O 1s, Pt 4f, C 1s, N 1s and Ni $2p_{3/2}$ core levels.

Elements	5 s	10 s	20s	Assignment
O1s	530.9 eV	530.6 eV	531.3 eV	Organic C-O
	533.4 eV	532.8 eV	533.4 eV	Organic C=O
	535.4 eV			
Pt4f	71.9 eV	71.1 eV	72.2 eV	Pt^0 metal
	73.0 eV	72.3 eV	73.4 eV	Pt^{2+}
	75.2 eV	74.4 eV	75.4 eV	Pt^0 satellite peaks
	77.2 eV	76.4 eV	77.4 eV	Pt^{2+} satellite peaks
C1s	284.8 eV	284.8 eV	284.8 eV	Organic C-C
	286.4 eV	286.6 eV	286.2 eV	Organic C-O or C-N
	287.9 eV		288.0 eV	Organic C=O
N1s			398.4 eV	M-N bond
	399.1 eV	398.8 eV		
	400.3 eV	400.3 eV	400.7 eV	$C\text{-}NH_2$
N2p$_{3/2}$	853.2 eV	852.7 eV	853.4 eV	Ni^0 metal
	855.0 eV		855.4 eV	Ni-OH (Ni^{2+})
		857.2 eV	857.7 eV	Ni^0 satellite peaks

6. In-situ Heating Studies

The particles formed after 5, 7.5, and 10 seconds were studied for their stability by heating them from room temperature to 1100°C under ultra-high vacuum in a probe-corrected FEI Titan G2 80-300 ST. The temperature was controlled using a Protochips Aduro holder.

The nanoparticles formed after 10 seconds showed the onset of aggregation of particles above 600°C (Figure S14), but overall retained their faceting and cuboctahedral nature up to 1100°C (Figure S14 and S15). This observation is consistent with the work of Wen *et al.* on the theoretically stable forms of platinum nanoparticles at elevated temperature.[6] After 3 hours at 1100°C, the particles are 3 ± 1 nm with the increase in size distribution being attributed to the formation of the larger aggregated particles (Figure S14, red arrows).

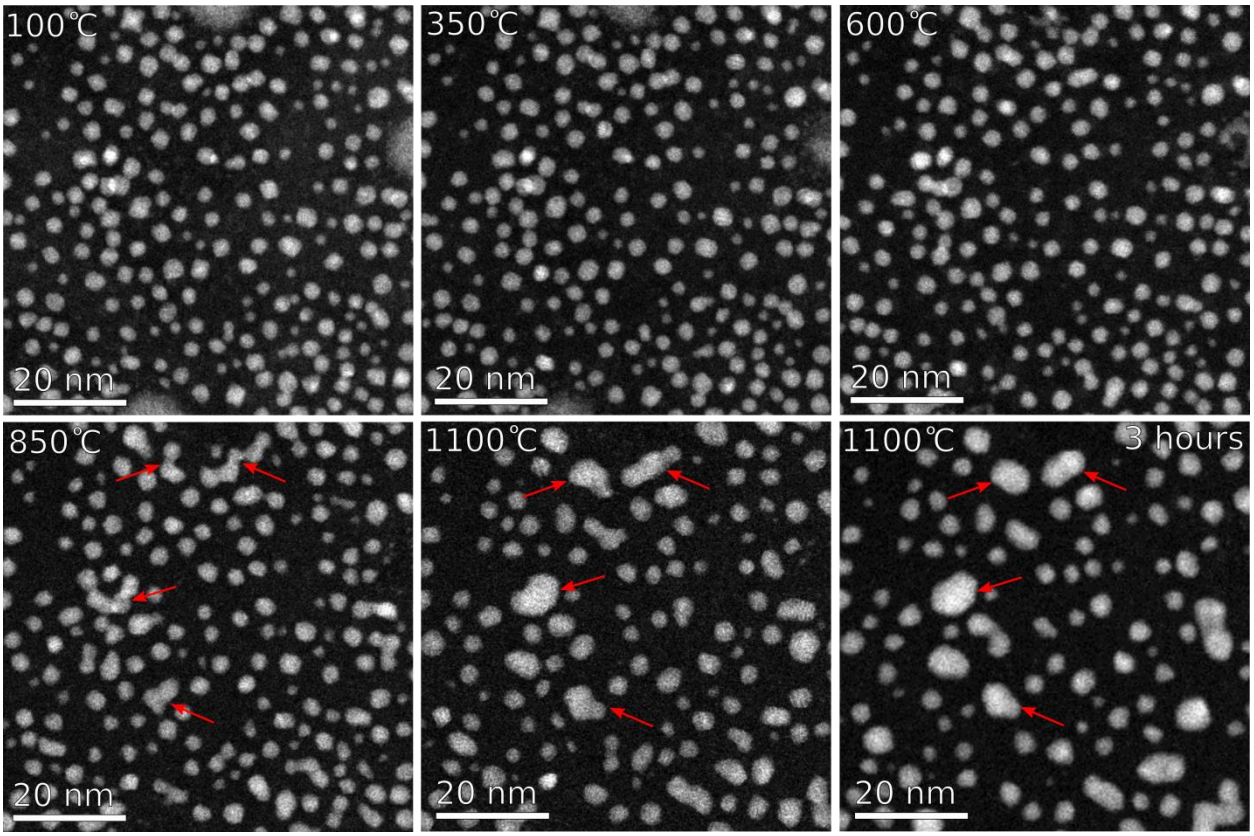

Figure S14. Platinum nickel nanoparticles from the 10 second sample at temperatures from 100°C to 1100°C, and held there for 3 hours. The red arrows show some of the areas where the touching particles have begun to sinter (850°C) and then completely combine into a single particle (1100°C).

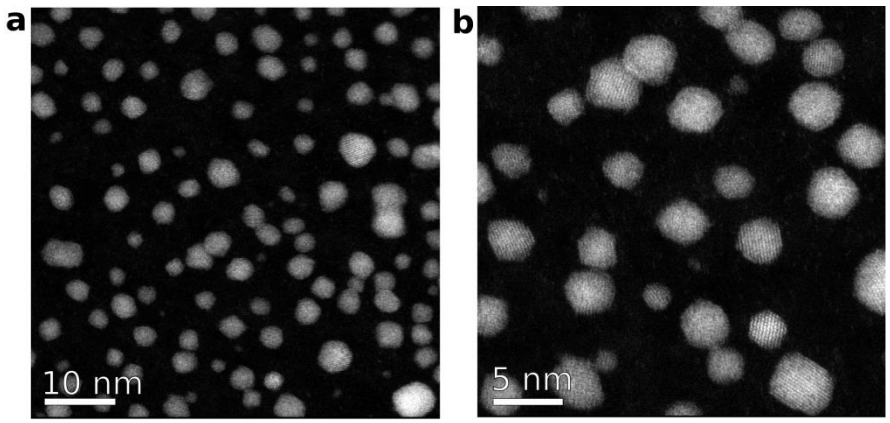

Figure S15. Platinum nickel nanoparticles from the 10 second sample at 1100°C showing the faceted nature of the remaining particles at two different magnifications, **a**) and **b**).

For the particles formed after 7.5 seconds, at 500°C, the particle size is 1.6 ± 0.4 nm and is still faceted (Figure S16). By 850°C the particles are 2.0 ± 0.7 nm, and aggregation has dominated the ripening and size broadening of the particles (Figure S16). Although, some Ostwald ripening was also observed (Figure S17). After 3 hours at 1100°C the particle size increased to 3 ± 1 nm (Figure S16). The effect of the electron beam was minimized by exposing the particles to the electron beam only during image acquisition.

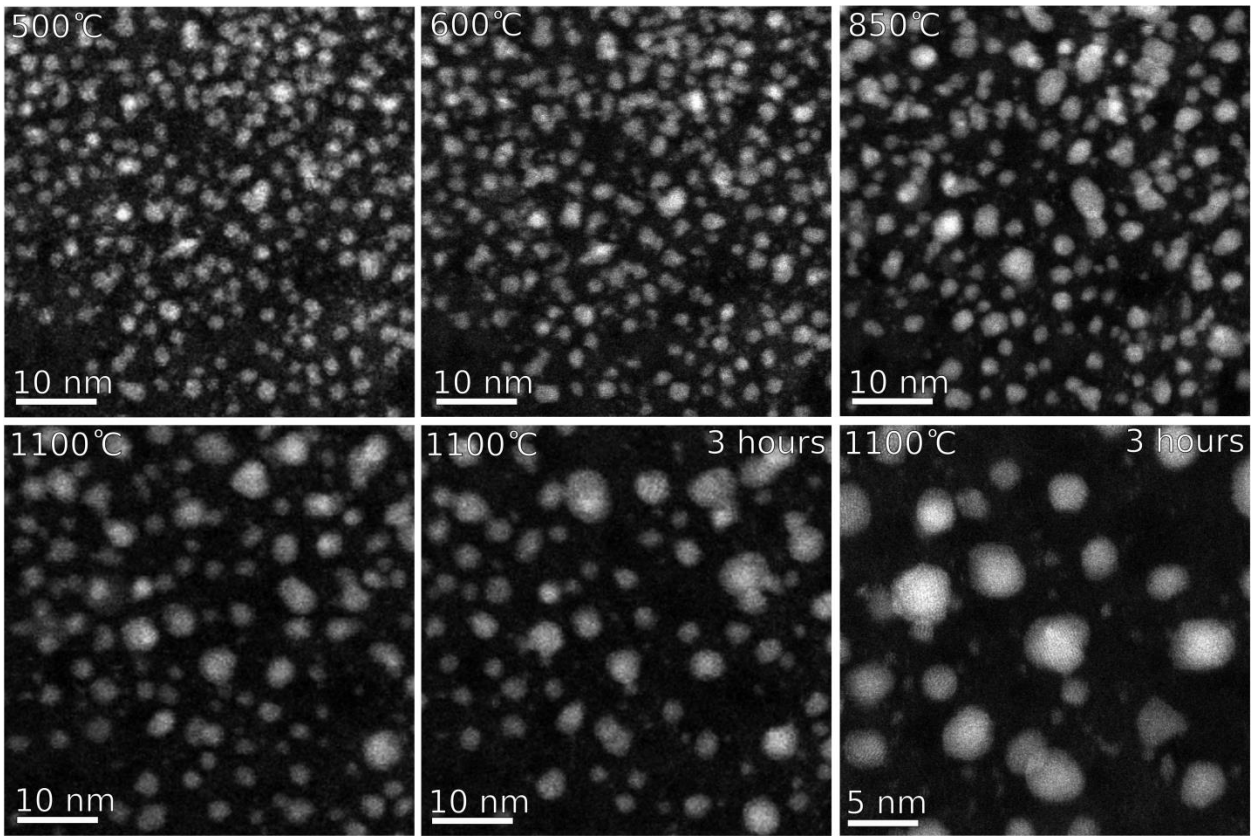

Figure S16. Platinum nickel nanoparticles from the 7.5 second sample at temperatures from 500°C to 1100°C, and held there for 3 hours.

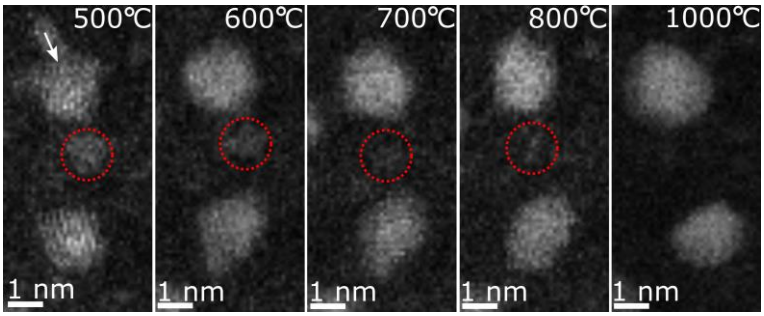

Figure S17. Platinum-nickel nanoparticles from the 7.5 second sample, at temperatures from 500°C to 1000°C looking at the decay of a small nanoparticle (in the dotted red circle), as the two larger particles get bigger. The white arrow shows coalescence of a small nanoparticle is shown into a larger nanoparticle at 500°C.

The sample formed after 5 seconds shows a mixture of single atoms, poorly ordered particles and crystalline particles with very similar size distributions (Figure S18).

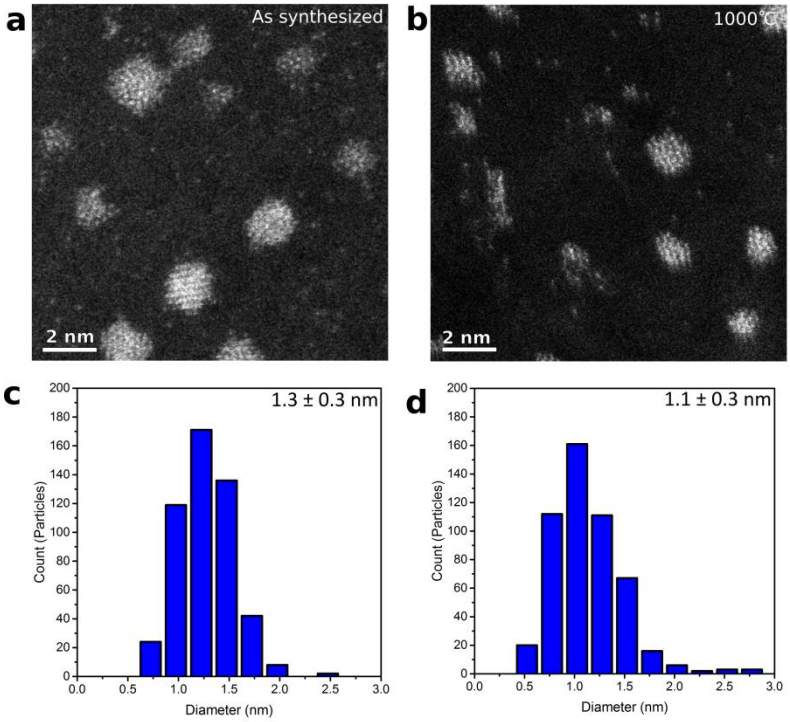

Figure S18. Platinum-nickel nanoparticles from the 5 second sample as synthesized (a) and heated to 1000°C (b) showing the nature of the particles remaining and their subsequent size distributions respectively in c) and d).

7. Other Metals and Alloys

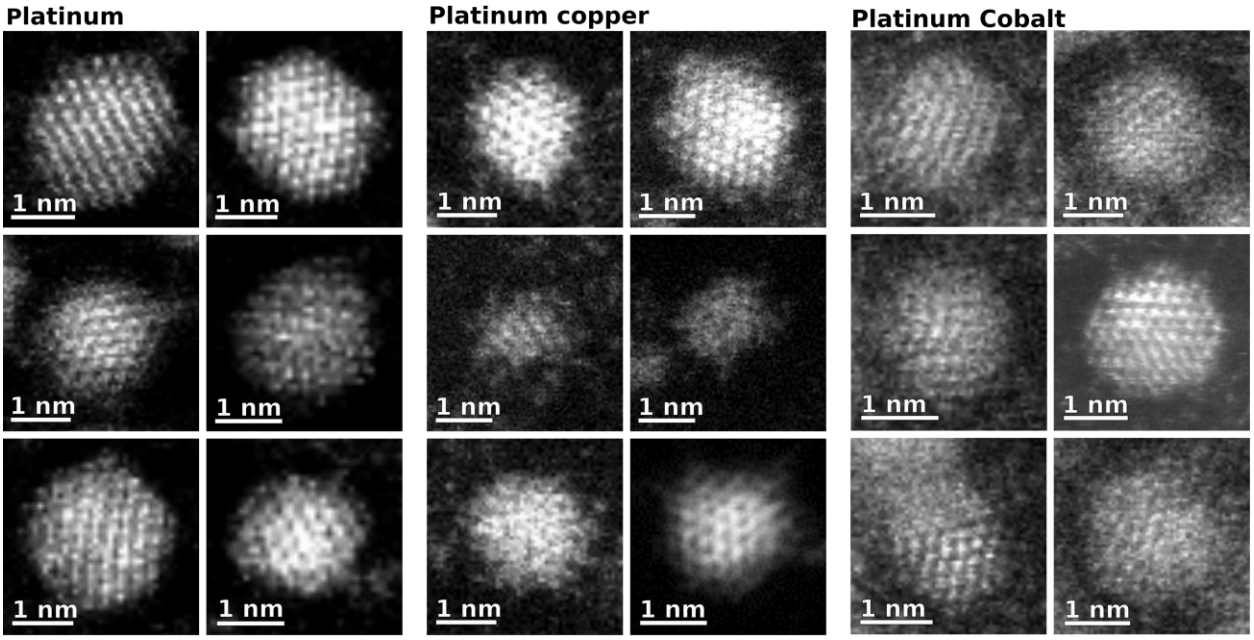

Figure S19. High resolution HAADF-STEM images of the platinum particles formed after 5 seconds, the platinum-copper particles formed after 10 seconds, and the platinum-cobalt particles formed after 5 seconds.

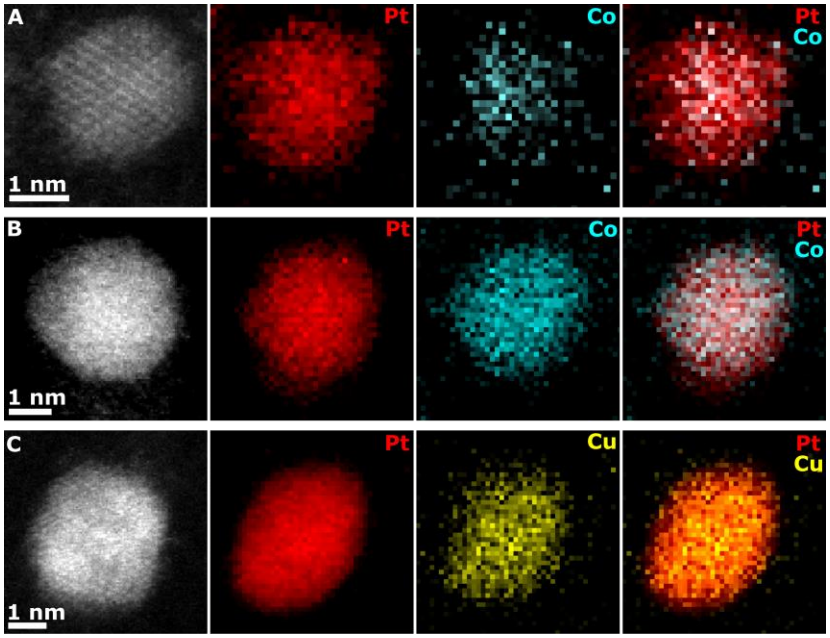

Figure S20. EELS maps of the A) 2.2 nm platinum-cobalt, B) 4.0 nm platinum-cobalt and a C) 3.5 nm platinum-copper particle. The maps in C) are elongated due to sample drift during acquisition.

8. References

1 A. P. LaGrow, B. Ingham, M. F. Toney and R. D. Tilley, *J. Phys. Chem. C*, 2013, **117**, 16709-16718.

2 A. P. LaGrow, K. R. Knudsen, N. M. AlYami, D. H. Anjum and O. M. Bakr, *Chem. Mater.*, 2015, **27**, 4134-4141.

3 B. Demeler and K. E. van Holde, *Anal. Biochem.*, 2004, **335**, 279-288.

4 L. Vitos, A. V. Ruban, H. L. Skriver and J. Kollár, *Surf. Sci.*, 1998, **411**, 186-202.

5 Y. Xia, Y. Xiong, B. Lim and S. E. Skrabalak, *Angew. Chem. Int. Ed.*, 2009, **48**, 60-103.

6 Y. Wen, H. Fang, Z. Zhu and S. Sun, *Phys. Lett. A*, 2009, **373**, 272-276.

7 V. M. Burlakov and L. Kantorovich, *J. Chem. Phys.*, 2011, **134**, 024521.

8 B. Demeler, in *Modern Analytical Ultracentrifugation: Techniques and Methods*, eds. D. J. Scott, S. E. Harding and A. J. Rowe, The Royal Society of Chemistry, Lindon, Editon edn., 2005, pp. 210-229.

9 T. M. D. Besong, S. E. Harding and D. J. Winzor, *Analytical Biochemistry*, 2012, **421**, 755-758.

10 E. Brookes, W. Cao and B. Demeler, *European biophysics journal : EBJ*, 2010, **39**, 405-414.

11 W. Peng, R. Mahfouz, J. Pan, Y. Hou, P. M. Beaujuge and O. M. Bakr, *Nanoscale*, 2013, **5**, 5017-5026.